

Emergent quantum phases in a frustrated J_1 - J_2 Heisenberg model on hyperhoneycomb lattice

SungBin Lee,¹ Jae-Seung Jeong,² Kyusung Hwang,¹ and Yong Baek Kim^{1,2}

¹*Department of Physics, University of Toronto, Toronto, Ontario M5S 1A7, Canada*

²*School of Physics, Korea Institute for Advanced Study, Seoul 130-722, Korea*

(Dated: February 28, 2022)

We investigate possible quantum ground states as well as the classical limit of a frustrated J_1 - J_2 Heisenberg model on the three-dimensional (3D) hyperhoneycomb lattice. Our study is inspired by the recent discovery of β -Li₂IrO₃,¹ where Ir⁴⁺ ions form a 3D network with each lattice site being connected to three nearest neighbors. We focus on the influence of magnetic frustration caused by the second-nearest neighbor spin interactions. Such interactions are likely to be significant due to large extent of 5d orbitals in iridates or other 5d transition metal oxides. In the classical limit, the ground state manifold is given by line degeneracies of the spiral magnetic-order wavevectors when $J_2/J_1 \gtrsim 0.17$ while the collinear stripy order is included in the degenerate manifold when $J_2/J_1 = 0.5$. Quantum order-by-disorder effects are studied using both the semi-classical $1/S$ expansion in the spin wave theory and Schwinger boson approach. In general, certain coplanar spiral orders are chosen from the classical degenerate manifold for a large fraction of the phase diagram. Nonetheless quantum fluctuations favor the collinear stripy order over the spiral orders in an extended parameter region around $J_2/J_1 = 0.5$, despite the spin-rotation invariance of the underlying Hamiltonian. This is in contrast to the emergence of stripy order in the Heisenberg-Kitaev model studied earlier on the same lattice, where the Kitaev-type Ising interactions are important for stabilizing the stripy order.²⁻⁴ As quantum fluctuations become stronger, U(1) and Z₂ quantum spin liquid phases are shown to arise via quantum disordering of the Néel, stripy and spiral magnetically-ordered phases. The effects of magnetic anisotropy and their relevance to future experiments are also discussed.

I. INTRODUCTION

Recent research activities on 5d transition metal oxides suggest that the strong spin-orbit coupling in conjunction with electron correlation may lead to unusual topological and magnetic phases.⁵⁻¹⁴ In particular, it has been recognized that the band-width of spin-orbit-reorganized bands near the Fermi level often becomes relatively narrow and moderate strength of electron correlation may be enough to generate Mott insulators. In such 5d Mott insulators, however, one would expect that spin exchange interactions between lattice sites beyond nearest-neighbors would become significant due to the extended nature of 5d orbitals. In addition, many of these Mott insulators are the so-called weak Mott insulators with a small charge gap and significant local charge fluctuations can generate multi-spin exchange interactions around multiple lattice sites.¹⁴⁻¹⁸ These further neighbor spin interactions, for example, may provide magnetic frustration and lead to emergence of quantum spin liquid and/or other exotic phases. On the other hand, various forms of anisotropic spin interactions may also be present due to spin-orbit coupling. The interplay between anisotropic spin interactions and the magnetic frustration effect is of fundamental importance in understanding quantum magnetism in 5d transition metal oxides.

The layered two-dimensional (2D) honeycomb iridates, Na₂IrO₃ and Li₂IrO₃, are fertile playgrounds, where the combined effects of anisotropic spin interactions and extended nature of 5d orbitals have been intensively studied.^{6,10-12,19} For example, it is shown that the so-called Kitaev model with bond-dependent anisotropic spin interactions may arise in the strong Mott regime. This has raised the hope that a quantum spin liquid phase, the exact solution of the model, may be realized.^{20,21} However, the ground state phase diagram of the Kitaev-Heisenberg model, where the Kitaev term is supplemented by the antiferromagnetic nearest-neighbor Heisenberg

interaction, is not fully consistent with the magnetic orders discovered in Na₂IrO₃ and Li₂IrO₃. It has been suggested that further neighbor spin interactions due to the large extent of 5d orbitals may also be important for the explanation of the experimental results.^{22,23} Which interaction would play the dominant role for the determination of magnetic order or ground state in real materials has been a subject of intensive debate.

In this paper, we study a frustrated J_1 - J_2 Heisenberg model on the three-dimensional (3D) hyperhoneycomb lattice, where Ir⁴⁺ ions reside in the newly discovered 3D iridate β -Li₂IrO₃.¹ Here J_1 and J_2 represent the nearest- and next-nearest neighbor exchange interactions. In the hyperhoneycomb lattice, each lattice site is connected to three neighboring sites just like the 2D honeycomb lattice. The ground state phase diagram of the Heisenberg-Kitaev model on this lattice has recently been studied and contains a number of collinear magnetic orders as well as a 3D quantum-spin-liquid in the Kitaev limit.^{2-4,24-26} Similarly to the 2D cousin, the full understanding of the magnetic phase diagram for β -Li₂IrO₃ would require the consideration of both Kitaev-like magnetic anisotropy and magnetic frustration due to further neighbor exchange interactions. In this work, we mostly focus on the effect of the latter by studying the simplest frustrated spin model, where we consider the spin interactions between second nearest-neighbor sites that are connected to a common nearest neighbor site. As we show below, this minimal model is microscopically motivated and exhibits degenerate classical ground state manifold, a hallmark of frustrated magnets.

We first investigate the classical limit of this model and identify the degenerate classical ground state manifold. Then quantum order-by-disorder effects are studied using semi-classical spin-wave analysis via the $1/S$ expansion and Schwinger boson mean-field theory. In the classical limit, the Luttinger-Tisza and single-**Q** variational ansatz reveal various line degeneracies of ordering wave vectors for spiral magnetic

order when $J_2 \gtrsim 0.17J_1$. On the other hand, the Néel order is chosen for $J_2 \lesssim 0.17J_1$. Interestingly, the collinear stripy order is in the classical degenerate ground state manifold at a single point $J_2 = 0.5J_1$. This is due to the peculiar lattice geometry of the hyperhoneycomb lattice as discussed later.

Upon including zero-point quantum fluctuations via the $1/S$ expansion in the spin-wave analysis, quantum order by disorder effects lift the line degeneracies in the classical spiral order regimes and in general select certain coplanar spiral order. Surprisingly, the collinear stripy order wins over the spiral magnetic order for an extended region around $J_2/J_1 = 0.5$, not just at $J_2/J_1 = 0.5$. It is remarkable that quantum fluctuations favor a collinear stripy ordered state even though the underlying Hamiltonian is $SU(2)$ symmetric. This is in contrast to the emergence of the stripy order discovered earlier in the Heisenberg-Kitaev model on the same 3D lattice, where the anisotropic Ising-type spin interaction is important for the stabilization of the stripy order.^{2-4,24} This suggests that *if the stripy order were observed in experiments, it could have arisen from two completely different kinds of interactions*. The Schwinger boson analysis in the semi-classical limit corroborates the results of the $1/S$ expansion and provides the same general trend of the quantum order-by-disorder effect while the phase boundaries between different phases are not the same. When quantum fluctuations become stronger, the Schwinger boson mean-field theory predicts the existence of the $U(1)$ and Z_2 quantum spin liquid phases that can be obtained by quantum disordering the Néel, stripy and spiral magnetic ordered phases, respectively. Finally the effects of possible magnetic anisotropy on this model are investigated.

The rest of the paper is organized as follows. In Sec. II, we introduce the J_1 - J_2 Heisenberg model on the hyperhoneycomb lattice and discuss its symmetry properties. Using the Luttinger-Tisza and single- \mathbf{Q} variational methods, we determine the degenerate classical ground state manifold in Sec. III. In Sec. IV, we investigate quantum order-by-disorder effects on the degenerate spiral states by computing zero-point quantum fluctuations via $1/S$ expansion and solving Schwinger boson mean-field theory. We show the emergence of stripy order due to quantum fluctuations. Moreover, possible spin liquid phases in the presence of strong quantum fluctuations are examined using the Schwinger boson analysis. We conclude in Sec. V with a summary of our results and discussion on magnetic anisotropy effect.

II. J_1 - J_2 HEISENBERG MODEL ON THE HYPERHONEYCOMB LATTICE

We start by introducing the J_1 - J_2 Heisenberg spin model on the hyperhoneycomb lattice. The model Hamiltonian is written as

$$\mathcal{H} = J_1 \sum_{\langle ij \rangle} \mathbf{S}_i \cdot \mathbf{S}_j + J_2 \sum_{\langle\langle ij \rangle\rangle} \mathbf{S}_i \cdot \mathbf{S}_j, \quad (1)$$

where $\langle ij \rangle$ and $\langle\langle ij \rangle\rangle$ run over the nearest-neighbor and next-nearest-neighbor bonds, respectively. Figure 1 shows the hyperhoneycomb lattice structure with four sublattices. Differ-

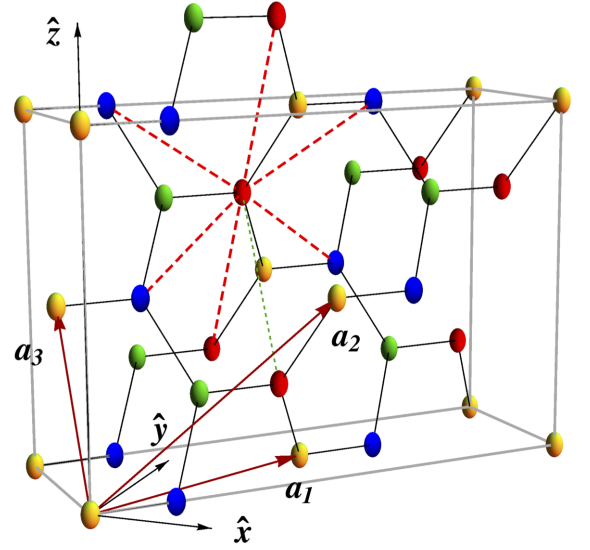


FIG. 1. (Color online) The hyperhoneycomb lattice structure with tri-coordinated four sublattices (yellow, blue, green, and red spheres). \mathbf{a}_i ($i = 1, 2, 3$, red arrows) denote the primitive lattice vectors for the face-centered orthorhombic Bravais lattice. Black solid lines show the nearest-neighbor bonds and red dashed lines indicate the next-nearest-neighbors that are connected via two nearest-neighbor bonds. Green dotted line has the same length as the distance between the next-nearest-neighbors connected by red dashed lines, but two sites coupled by green dotted lines are not connected via two nearest-neighbor bonds.

ent sublattice sites labeled by $s = 0, 1, 2, 3$ are colored in yellow, blue, green and red. This three-dimensional lattice can be regarded as a face-centered orthorhombic Bravais lattice with a four-site basis (See Appendix A for details). Notice that each site is connected to three nearest-neighbor sites, just like the 2D honeycomb lattice.

The nearest-neighbor bonds connect two kinds of sublattices, namely even ($s = 0, 2$) and odd sublattices ($s = 1, 3$). On the other hand, there are six next-nearest-neighbors connected via two nearest-neighbor bonds through a common nearest-neighbor site [red dashed lines in Fig. 1]. The connection amongst the next-nearest-neighbors exists only between even and even, or odd and odd sublattices. Such special connectivity leads to the J_1 - J_2 Heisenberg Hamiltonian \mathcal{H} in Eq.(1) to be invariant under the following transformation

$$\mathbf{S}_i^{0,2(1,3)} \rightarrow -\mathbf{S}_i^{0,2(1,3)}, \quad J_1 \rightarrow -J_1, \quad (2)$$

where \mathbf{S}_i^α corresponds to \mathbf{S}_i located on the sublattice α at site i spanned by the primitive lattice vectors. Notice that the sign change of the nearest-neighbor exchange coupling J_1 is equivalent to that of the spin on either even or odd sublattices. Hence, without losing generality, one can explore either ferromagnetic or antiferromagnetic sides of the magnetic phase diagram for J_1 (i.e. $J_1 < 0$ or $J_1 > 0$), then the other side of the phase diagram is automatically determined, followed by the transformation in Eq. (2). Throughout this paper, we assume $J_1, J_2 > 0$ unless specified otherwise. In addition to six next-nearest-neighbors connected by two nearest-

neighbor bonds, there are other four next-nearest-neighbors with the same lattice distance [green dotted line in Fig. 1], but not being connected by two nearest-neighbor bonds. Previous microscopic consideration of the underlying tight-binding model suggests that the spin exchange interactions for the six next-nearest-neighbors are dominant and those for the four extra next-nearest-neighbors is negligible for edge-sharing oxygen octahedra environment of Ir^{4+} ions.²⁷ Hence, we focus on six next-nearest-neighbors that are connected by two nearest-neighbor bonds.

III. MAGNETIC PHASE DIAGRAM IN THE CLASSICAL LIMIT

We first explore the classical ground states of the antiferromagnetic J_1 - J_2 Heisenberg model [Eq. (1)] on the hyperhoneycomb lattice. Using two different approaches: Luttinger-Tisza and single- \mathbf{Q} variational analyses, we determine the degenerate classical-ground-state manifold. When $J_2 \gtrsim 0.17J_1$, we find line degeneracies of the wavevectors for spiral ordered phases while the Néel order is the ground state for $J_2 < 0.17J_1$. Notably at a single point $J_2 = 0.5J_1$, the collinear stripy order coexists with spiral orders in the degenerate ground state manifold, which is shown to arise from the peculiar lattice geometry of the hyperhoneycomb lattice. We explain below the results of the Luttinger-Tisza approach and single- \mathbf{Q} variational ansatz.

A. Luttinger-Tisza method

In the nearest-neighbor antiferromagnetic Heisenberg model (for $J_1 > 0$, $J_2 = 0$), the Néel order is the unique ground state, where spins in even and odd sublattices are pointing opposite directions. However, when J_2 becomes finite and comparable to the strength of J_1 , two exchange interactions compete with each other and may induce non-trivial magnetic order. In this section, we adopt the Luttinger-Tisza analysis and investigate frustration-induced magnetic phases in the classical limit. The Luttinger-Tisza method^{28–30} finds the ordering wavevectors of classical spin ground states by minimizing the energy of \mathcal{H} [Eq. (1)], where the spin is regarded as a classical three-component unit-vector. The solutions are typically found in a mean-field fashion in the sense that the hard spin constraint, $|\mathbf{S}_i| = 1$ at every site i , is only satisfied on average or a soft spin constraint, $\sum_{i \in uc} |\mathbf{S}_i|^2 = N_s$ (uc = unit cell and $N_s = 4$ is the number of sites in the unit cells) is used. While the solutions include the true ground state manifold, some of the solutions may fail to satisfy the hard spin constraint. Hence, we first look for the Luttinger-Tisza solutions with the soft spin constraint and then find the true ground state manifold among them by examining the hard spin constraint.

Based on the Luttinger-Tisza analysis, we find that the Néel order with the ordering wavevector at the Γ point, is the ground state for $J_2/J_1 \lesssim 0.17$. For $J_2/J_1 \gtrsim 0.17$, on the other hand, the competition between J_1 and J_2 leads to de-

generate spiral states, with the ordering wavevectors located away from the Γ point. Within the soft spin constraint, the degenerate ordering wavevectors, that minimize the energy of \mathcal{H} [Eq. (1)], form a surface in the wavevector space. Figure 2 shows such degenerate surfaces (colored in blue) of the ordering wavevectors in the first Brillouin zone. For different values of $J_2/J_1 = 0.2, 0.3, 0.5$ and 0.7 , the degenerate surfaces are shown in each panel of Figs. 2 (a)-(d), respectively. We find degenerate surfaces with different topologies depending on the ratio of J_2/J_1 . The degenerate wavevectors form closed surfaces in the range $0.17 \lesssim J_2/J_1 \lesssim 0.2$ and one of them is shown in Fig. 2 (a) for $J_2/J_1 = 0.2$. As J_2/J_1 increases further, open surfaces emerge as shown in Figs. 2 (b), (c), and (d). Notice that the open surface at $J_2/J_1 = 0.5$ has a touching point at Γ , which means that collinear ordered phase with $\mathbf{q} = 0$ is a part of the solutions. It is also interesting that open surfaces have distinct topologies for $0.2 \lesssim J_2/J_1 < 0.5$ and $J_2/J_1 > 0.5$. These behaviors stem from a special property of the hyperhoneycomb lattice structure. It will be shown later that this special property is related to the emergence of collinear stripy order near $J_2/J_1 = 0.5$ upon including quantum fluctuations. This will be discussed in details in Sec. III B and Sec. IV.

Now we determine the true classical ground-state manifold by examining which solutions on the degenerate surfaces would satisfy the hard spin constraint. Careful investigations reveal that only special lines of the ordering wavevectors on the degenerate surfaces satisfy the hard spin constraint. Black lines in Figs. 2 (a)-(d) represent the ordering wavevectors that meet the hard spin constraint for different values of J_2/J_1 . In general, the degenerate lines lie on the two planes ΓZTY and ΓXAZ where the Γ , Z , T , Y , X , and A respectively indicate the high symmetry points in the Brillouin zone (See Appendix A for details). When degenerate surfaces intersect with the Brillouin zone boundary, however, there are extra degenerate lines at the zone boundary perpendicular to the $\hat{\mathbf{q}}_z$ axis as shown in Figs. 2 (b), (c) and (d). These solutions with degenerate lines are shown to be consistent with the results of the single- \mathbf{Q} variational approach as discussed in the next section.

B. Single- \mathbf{Q} variational approach

As an alternative approach, we use a variational ansatz for the classical solutions that satisfy the hard spin constraint explicitly. Treating the spins as classical three-component unit-vectors, we consider the following single- \mathbf{Q} variational ansatz.

$$\mathbf{S}_i = \mathcal{R}e[\mathbf{d} e^{i(\mathbf{Q} \cdot \mathbf{r}_i + \varphi_s)}], \quad \mathbf{d} = \hat{\mathbf{e}}_1 + i\hat{\mathbf{e}}_2, \quad (3)$$

with variational parameters \mathbf{Q} and φ_s , where \mathbf{Q} is the ordering wavevector and φ_s is a sublattice- s -dependent phase factor. Here, $\hat{\mathbf{e}}_1$ and $\hat{\mathbf{e}}_2$ are orthogonal unit vectors and they can be freely chosen as the underlying Hamiltonian is $\text{SU}(2)$ invariant. Using the variational ansatz in Eq. (3), we find the parameter values of \mathbf{Q} and φ_s that minimize the energy of the

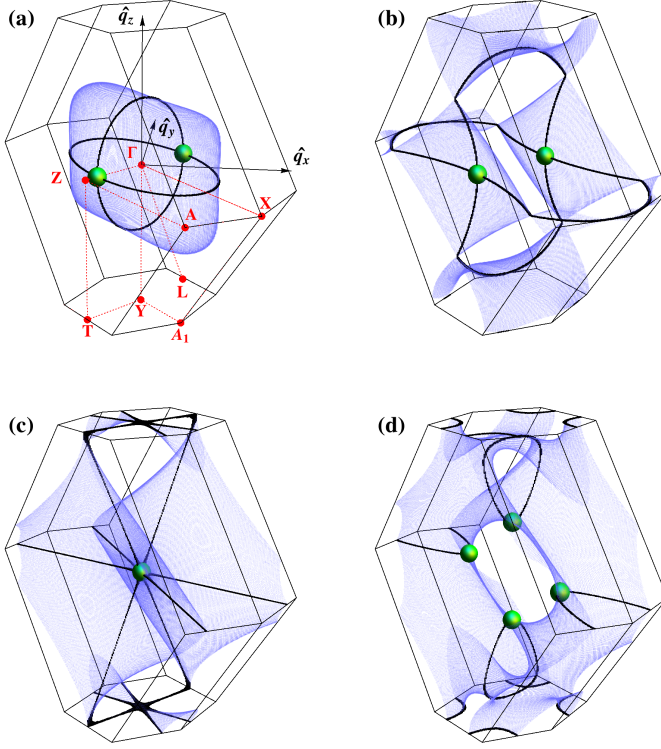


FIG. 2. (Color online) Ordering wavevectors of the classical solutions obtained in the Luttinger-Tisza analysis with the soft spin constraint are shown as degenerate surfaces (blue) for (a) $J_2/J_1 = 0.2$, (b) $J_2/J_1 = 0.3$, (c) $J_2/J_1 = 0.5$, and (d) $J_2/J_1 = 0.7$. Black lines on the degenerate surfaces denote the ordering wavevectors of the classical spin states that satisfy the hard spin constraint. These degenerate lines of wavevectors are consistent with the results of the single- \mathbf{Q} variational method [see Sec. III B]. Green spheres represent the selected ordering wavevectors in the presence of zero-point quantum fluctuations. [see Sec. IV A for details]

J_1 - J_2 Heisenberg spin Hamiltonian \mathcal{H} [Eq. (1)]. This variational ansatz always satisfies the hard spin constraint $|\mathbf{S}_i| = 1$, but works only when the magnetic ordering is described by a single wavevector. Black lines in Figs. 2 (a)-(d) show the wavevectors \mathbf{Q} , which minimize \mathcal{H} [Eq. (1)] for different values of J_2/J_1 . We note that these single- \mathbf{Q} solutions are fully consistent with the ones of the Luttinger-Tisza analysis supplemented with the hard spin constraint. Below we point out a number of important characteristics of these classical spin states that form the line degeneracies.

(i) Magnetic frustration induced by the competition between J_1 and J_2 in the hyperhoneycomb lattice leads to a manifold of “spiral line states”, where degenerate ordering wavevectors form lines in the 3D Brillouin zone. It is interesting to compare this line degeneracy with the classical ground states of the same Heisenberg model on the 3D diamond lattice, where the ordering wavevectors form degenerate surfaces in the Brillouin zone or represent “spiral surface states”.^{31,32} The diamond lattice contains two sublattices

in the unit cell and the nearest-neighbors (next-nearest-neighbors) connect different (same) sublattices. When $J_1 > 0$ and $J_2 = 0$, the ground state is clearly the Néel state with the ordering wavevector $\mathbf{Q} = 0$. In the case of $J_1 = 0$ and $J_2 > 0$, on the other hand, magnetic frustration is present and degenerate classical spin states are characterized by ordering wavevectors aligned along any of three principal axes $\mathbf{Q} \parallel [100], [010], [001]$. Notice that all three principal directions in three-dimensions are equally allowed in this degenerate manifold. It is, therefore, natural to expect that the degenerate wavevectors of spiral states in the presence of both J_1 and J_2 would not exclusively occur on any particular plane or along a particular direction and rather form a degenerate surface. In contrast, the next-nearest-neighbors on the hyperhoneycomb lattice are connected between not only the same sublattices but also different ones. When $J_2 > 0$ and $J_1 = 0$, there exists magnetic frustration as in the case of the diamond lattice. However, the different connectivity for the next-nearest-neighbors leads to the degenerate wavevectors forming a circle on the $\Gamma X A_1 Y$ plane in the J_2 -only model. In this case, the next-nearest-neighbor interactions already determine a special plane on which the degeneracy of the wavevectors resides. Hence, one would expect that the degenerate wavevectors in the presence of both J_1 and J_2 would not form a surface spanning all three directions in the Brillouin zone and rather form degenerate lines/circles extended along two directions in a plane.

For the SU(2) invariant systems, the spiral plane on which the spins lie, can be freely chosen. In crystals, however, this SU(2) symmetry can be easily broken by the crystal lattice potential combined with the spin-orbit coupling. The spin-orbit effect couples the spin and spatial rotations allowed by the lattice symmetry. This may induce magnetic anisotropies and lock the spiral plane to be pointing along a special direction, depending on the ordering wavevectors. Notably, iridium electrons have strong spin-orbit coupling and certain magnetic anisotropies are likely to be present. In Sec. V, we discuss how such anisotropy effects select a particular spiral plane, depending on the ordering wavevectors.

(ii) At $J_2/J_1 = 0.5$, the line degeneracy of the classical ground state manifold contains not only spiral ordered phases, but also the collinear stripy phase with the ordering wavevector $\mathbf{Q} = 0$, where the spins in sublattices $\{0, 1\}$ and $\{2, 3\}$ point in opposite directions to each other (See Fig. 4 (c) for a schematic picture of the stripy order). When $J_2/J_1 = 0.5$, the ratio of J_2/J_1 becomes exactly the same as the ratio of the number of nearest neighbor bonds and that of next-nearest neighbor bonds, which are three and six respectively. The stripy order allows only 2/3 of the nearest-neighbor bonds to gain the antiferromagnetic spin exchange energy. However, it also gains the antiferromagnetic spin exchange energy for 2/3 of the next-nearest-neighbor bonds. As a result, the bond energies associated with J_1 and J_2 become equal at $J_2/J_1 = 0.5$, making the energy of the collinear stripy phase degenerate with those of competing spiral ordered phases. In the following section (Sec. IV), we explore the effects of quantum fluctuations using two different approaches: the $1/S$ expansion in the linear spin-wave theory and Schwinger boson mean-field

method. In particular, we show that the stripy order wins over the competing spiral ordered phases in a finite range of parameters near $J_2/J_1 = 0.5$ upon including quantum fluctuations, despite the fact that the stripy phase is a part of the classical ground state manifold only at $J_2/J_1 = 0.5$.

IV. QUANTUM ORDER-BY-DISORDER, EMERGENCE OF STRIPY PHASE, AND QUANTUM SPIN LIQUIDS

Quantum fluctuation may lift the line degeneracy in the classical-ground-state manifold, identified in the previous section. This *quantum order-by-disorder* effect may select certain magnetically ordered phase among the degenerate ground states. When quantum fluctuations become extremely strong, however, magnetic ordering would be completely suppressed and various quantum spin liquid phases may become emergent ground states. Here we explore both possibilities using two different approaches.

In Sec. IV A, we first use the large- S analysis of the linear spin wave theory to investigate quantum order-by-disorder effects by computing zero-point quantum-fluctuation energy of degenerate classical ground states. We show that, in general, quantum fluctuations select certain magnetically ordered phases with ordering wavevectors lying along the high symmetry directions in the Brillouin zone. It is also found that quantum fluctuations favor collinear ordered states such as the Néel and stripy phases in a much wider region of the parameter space, compared to the classical limit. In Sec. IV B, it is shown that the Schwinger boson approach results in similar quantum order-by-disorder effects. We also explore emergent quantum spin liquid phases in the Schwinger boson mean-field theory when quantum fluctuations are very strong.

A. Large- S analysis

We now consider the linear spin-wave theory via the Holstein-Primakoff boson representation. In order to include quantum fluctuations, we adopt the following spin-coordinate frame at each site i .

$$\begin{aligned}\hat{z}_i &= \hat{S}_i^{\text{cl}} = \mathcal{R}e[\mathbf{d} e^{i(\mathbf{Q} \cdot \mathbf{r}_i + \varphi_s)}], \\ \hat{x}_i &= -\mathcal{I}m[\mathbf{d} e^{i(\mathbf{Q} \cdot \mathbf{r}_i + \varphi_s)}], \\ \hat{\mathbf{y}} &= \frac{i}{2} \mathbf{d} \times \mathbf{d}^* = \hat{\mathbf{e}}_3,\end{aligned}\quad (4)$$

where the local \hat{z}_i axis is defined to be parallel to the direction of the classical spin order [See Eq.(3)]. For coplanar spiral states, one of the coordinate axis, $\hat{\mathbf{y}}$, can be taken as the normal vector of the spiral plane and it would be site-independent. In the large- S limit, the linearized Holstein-Primakoff transformation can be written as

$$\mathbf{S}_i = (S - n_i)\hat{z}_i + \sqrt{2S} \left(a_i^\dagger \frac{\hat{x}_i + i\hat{\mathbf{y}}}{2} + a_i \frac{\hat{x}_i - i\hat{\mathbf{y}}}{2} \right), \quad (5)$$

where S is the spin magnitude, $a_i^\dagger (a_i)$ are boson creation (annihilation) operators, and $n_i = a_i^\dagger a_i$ is the boson density operator. Using Eq.(5), we expand \mathcal{H} in Eq.(1) up to the quadratic

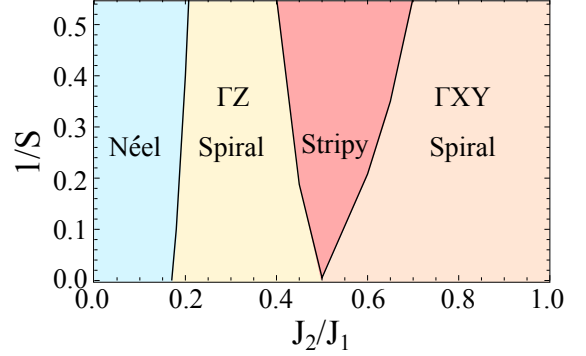


FIG. 3. (Color online) Magnetic phase diagram of the J_1 - J_2 Heisenberg model on the hyperhoneycomb lattice as a function of inverse spin magnitude $1/S$ and the ratio J_2/J_1 , where zero-point quantum fluctuations are included in the linear spin-wave theory. Notice that the collinear orders such as the stripy and Néel phases become the ground states for a wider region of parameter space as quantum fluctuations become stronger or $1/S$ becomes bigger.

order of boson operators, which results in the leading order Hamiltonian in the $1/S$ expansion. We can now easily evaluate the zero-point quantum fluctuation energy of the Holstein-Primakoff bosons (For more details, see Appendix B). One finds that quantum fluctuations select particular ordering wave vectors along the high symmetry lines of the Brillouin zone and such ordering wave vectors are depicted as green spheres in Figs. 2 (a)-(d) for different values of $J_2/J_1 = 0.2, 0.3, 0.5$ and 0.7 . Depending on parameter regions, different kinds of magnetically ordered phases are selected as follows.

- ΓZ spiral : For $0.17 \lesssim J_2/J_1 < 0.5$, quantum fluctuations select the ordering wavevectors $\mathbf{Q} = \pm q(1, 1, 0)$ along the Γ -Z line. Some examples are shown in Figs. 2 (a) and (b) for $J_2/J_1 = 0.2$ and $J_2/J_1 = 0.3$, respectively.
- ΓXY spiral : For $J_2/J_1 > 0.5$, quantum fluctuations favor the ordering wavevectors $\mathbf{Q} = \pm q(1, -1, 0)$ along the Γ -X line and $\mathbf{Q} = \pm q(0, 0, 1)$ along the Γ -Y line. Figure 2 (d) illustrates such selection of the ordering wavevectors for $J_2/J_1 = 0.7$.

Figure 3 shows the phase diagram as a function of inverse spin-magnitude $1/S$ and the ratio J_2/J_1 upon including zero-point quantum-fluctuation energy corrections. Notice that the collinear magnetic orders such as Néel and stripy phases, win over spiral orders in a wider range of parameter space as quantum fluctuations become stronger or $1/S$ becomes bigger. This is reminiscent of the same trend found in previous studies on various systems.³³⁻³⁵ For example, in the classical limit $S \rightarrow \infty$, the stripy phase is a part of the classical-ground-state manifold only at a single point $J_2/J_1 = 0.5$ (See Sec. III B for details). However, the collinear stripy phase becomes the ground state in a wider region of parameter space near $J_2/J_1 \sim 0.5$ when S becomes smaller. The same trend exists for the Néel phase, leading to a wider region of Néel order near $J_2/J_1 \sim 0.17$. Of course, the computations of

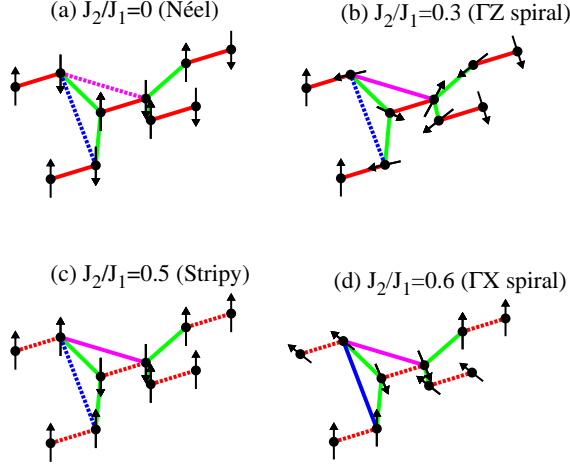


FIG. 4. (Color online) Classical spin configurations and Schwinger boson mean-field parameters. Spin moments are represented by arrows. Mean-field parameters η_n ($n = 1, 2, 3, 4$) in the Schwinger boson theory are denoted by red, green, blue, and magenta lines, respectively. Solid lines corresponds to antiferromagnetic correlations ($\eta_n > 0$) between two sites and dashed lines represent ferromagnetic arrangements ($\eta_n = 0$). For clarity, we show $\eta_{3,4}$ only on two J_2 -bonds in each figure with the rest of them being omitted.

zero-point quantum fluctuations in the linear spin-wave theory are valid only for large spin magnitude S or small $1/S$. In order to access the strong quantum fluctuation regime, we now turn to the Schwinger boson analysis that can be used to study both semi-classical and strongly quantum regimes on an equal footing.

B. Schwinger boson approach

In the Schwinger boson theory^{36–38}, the spin operator is represented in terms of spin-carrying bosons, $b_{i\alpha}$:

$$\mathbf{S}_i = \frac{1}{2} b_{i\alpha}^\dagger \boldsymbol{\sigma}_{\alpha\beta} b_{i\beta}, \quad (6)$$

where $\boldsymbol{\sigma}_{\alpha\beta}$ are the Pauli matrices ($\alpha, \beta \in \{\uparrow, \downarrow\}$), and summations over repeated Greek indices are assumed. Here the boson density at each site is related to the magnitude of the spin S via

$$n_b = b_{i\alpha}^\dagger b_{i\alpha} = \kappa, \quad (7)$$

where $\kappa = 2S$. Using the Schwinger boson representation, we consider the following mean-field Hamiltonian for the J_1 - J_2 Heisenberg model in Eq. (1).

$$\begin{aligned} \mathcal{H}_{MF} = & \sum_{i>j} \frac{J_{ij}}{2} \left(|\eta_{ij}|^2 - \eta_{ij} b_{i\alpha}^\dagger \epsilon_{\alpha\beta} b_{j\beta}^\dagger + \text{H.c.} \right) \\ & + \sum_i \lambda_i \left(b_{i\alpha}^\dagger b_{i\alpha} - \kappa \right), \end{aligned} \quad (8)$$

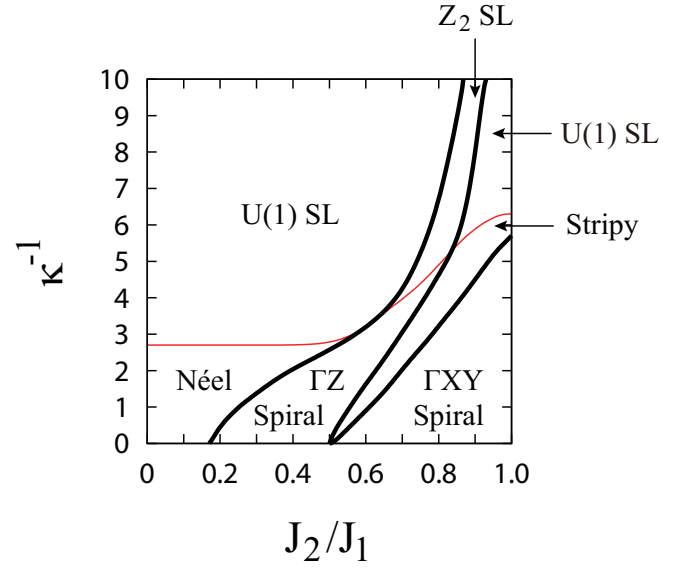


FIG. 5. (Color online) Mean-field phase diagram in the Schwinger boson theory. At small $1/\kappa$, quantum order-by-disorder effects select the Néel, ΓZ spiral, stripy, and ΓXY spiral phases. When quantum fluctuations become stronger (or $1/\kappa$ becomes bigger), U(1) and Z_2 quantum spin liquid phases arise. Thick solid (red thin) lines represent first (second) order phase transitions.

where $\eta_{ij} = \langle b_{i\alpha} \epsilon_{\alpha\beta} b_{j\beta} \rangle$ is the mean-field parameter ($\epsilon_{\alpha\beta}$ is the antisymmetric tensor) and λ_i is the Lagrange multiplier to implement the constraint on spin magnitude in Eq. (7). It has been known that such mean-field solutions become exact in the large- N limit of the $\text{Sp}(N)$ generalized model, where N flavors of bosons, $b_{i\alpha m}$ ($m = 1, 2, \dots, N$), are introduced and the constraint is generalized to $n_b = b_{i\alpha m}^\dagger b_{i\alpha m} = \kappa N$. The large- N limit is then taken by fixing $n_b/N = \kappa$. Notice that κ in this limit plays the role of $2S$ in the $\text{SU}(2)$ case, namely the large(small)- κ limit corresponds to semi-classical (quantum) regime. Thus the mean-field solution is *non-perturbative* in κ or $2S$ in contrast to the spin-wave theory. Here we directly work with the mean-field solutions in the $\text{SU}(2)$ limit. In this formulation, the bose condensation at large- κ leads to magnetically ordered phases while quantum spin liquid phases with gapped spin-carrying bosons, dubbed spinons, appear at small- κ . We explicitly include the condensate $x_{i\alpha} = \langle b_{i\alpha} \rangle$ degrees of freedom in Eq.(8) and minimize the energy $\langle \mathcal{H}_{MF} \rangle$ with respect to η_{ij} , λ_i , and $x_{i\alpha}$.

1. Classical limit and mean-field ansatz

The classical limit can be obtained by taking $\kappa \rightarrow \infty$ in the Schwinger boson mean-field theory, where the classical spins \mathbf{S}_i^c and mean-field link variables η_{ij}^c are written in terms of condensate amplitudes of bosons:

$$\mathbf{S}_i^c = \frac{1}{\kappa} x_{i\alpha}^* \boldsymbol{\sigma}_{\alpha\beta} x_{i\beta}, \quad (9)$$

$$\eta_{ij}^c = \frac{1}{\kappa} x_{i\alpha} \epsilon_{\alpha\beta} x_{j\beta}, \quad (10)$$

where the scaled \mathbf{S}_i and η_{ij} , normalized by the boson density κ , satisfy $|\mathbf{S}_i^c| = 1$ and $\mathbf{S}_i^c \cdot \mathbf{S}_j^c = -2|\eta_{ij}^c|^2 + 1$. Comparing Eqs. (9) and (10) with the single- \mathbf{Q} variational ansatz for the spiral spin states in Eq. (3), one can determine the corresponding expressions of $x_{i\alpha}$ and η_{ij} for the degenerate classical ground states investigated earlier. Upon including quantum fluctuations when κ is large and finite, we find that quantum order-by-disorder chooses the same set of magnetically ordered phases, namely Néel, Stripy, ΓZ , ΓXY spiral orders. It can be shown that the mean-field ansatz for these selected states requires four independent parameters η_n ($n = 1, \dots, 4$). Figures 4 (a)-(d) illustrate four different classical spin states: Néel, ΓZ spiral, stripy and ΓX spiral states. The corresponding mean-field parameters η_n ($n = 1, 2, 3, 4$) are also shown in the same figures. Colored solid lines indicate four different mean-field parameters η_n ($n = 1, 2, 3, 4$) for antiferromagnetic correlations and colored dashed lines represent ferromagnetic arrangement between two sites. The parameters $\eta_{1,2}$ are defined for the nearest-neighbor J_1 bonds and $\eta_{3,4}$ are for the next-nearest-neighbor J_2 bonds (see Appendix C for more details). As quantum fluctuations increase as κ becomes smaller, magnetically ordered phases are suppressed and the corresponding condensate densities of bosons vanish. This marks the transition to quantum spin liquid phases. In the next section, we explore the resulting phase diagram for various values of κ and J_2/J_1 .

2. Mean-field phase diagram

Figure 5 shows the mean-field phase diagram as a function of $1/\kappa$ and the ratio of J_2/J_1 . In the limit $\kappa \rightarrow \infty$, it successfully recovers all the classical magnetic phases with the phase boundaries consistent with the classical phase diagram. As an example, the behaviors of mean-field parameters as a function of J_2/J_1 for $1/\kappa = 2$ are shown in Fig. 6 (a). As shown in Fig. 4, the classical magnetic orders are described by different mean-field structures for various ranges of J_2/J_1 : (i) $\eta_{1,2} > 0$ for the Néel, (ii) $\eta_{1,2,4} > 0$ for the ΓZ spiral, (iii) $\eta_{2,4} > 0$ for the stripy, and (iv) $\eta_{2,3,4} > 0$ for the ΓXY spiral phases.

Just like the results of the linear spin-wave theory, the collinear orders such as the Néel and stripy phases exist in a wider region of the parameter space as quantum fluctuations become stronger or $1/\kappa$ becomes bigger. On the other hand, the phase boundaries between different phases look somewhat different, and this happens because quantum fluctuations enter differently in the linear spin-wave theory and Schwinger boson approach. At the mean-field level, the phase transitions between magnetically ordered phases at finite $1/\kappa$ are first order (black thick solid lines) as is evident from the behaviors of the mean-field parameters shown in Fig. 6.

When quantum fluctuations are further increased, second order phase transitions from the magnetically ordered phases to quantum spin liquid states occur at some critical $(1/\kappa)_c$. Quantum spin liquid phases for $1/\kappa > (1/\kappa)_c$ possess gapped bosonic spinon excitations. In the range of $0 \leq J_2/J_1 \leq 1$, we find $(1/\kappa)_c \simeq 3 - 6$. U(1) and Z_2 spin liquid phases arise for $1/\kappa > (1/\kappa)_c$ upon quantum disordering the Néel/stripy

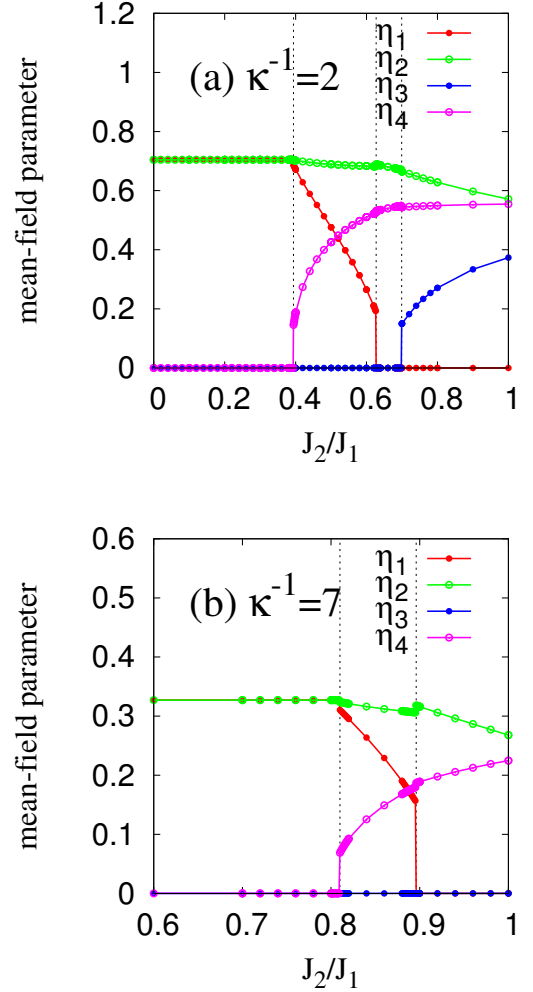


FIG. 6. (Color online) Mean-field parameters, $\{\eta_1, \eta_2, \eta_3, \eta_4\}$, as functions of J_2/J_1 at $1/\kappa = 2$ (magnetic order regime) and $1/\kappa = 7$ (spin liquid regime).

and spiral orders. As is well known, U(1) and Z_2 spin liquid phases typically occur via second order phase transition from collinear and spiral ordered phases, respectively. To be more specific, we show the behaviors of mean-field parameters for $1/\kappa = 7$ in Fig. 6 (b). Here U(1) and Z_2 refer to the gauge structure of quantum spin liquid phases, which can be characterized by physical quantities invariant under the corresponding gauge transformations. For example, the U(1) spin liquid arising from the Néel state is distinct from the U(1) spin liquid associated with the stripy order as gauge invariant quantities, such as the gauge-invariant products of link variables around closed loops,³⁹ are different in two phases.

Notice that the Z_2 spin liquid that emerges from the ΓZ spiral order (or the Z_2 spin liquid arising from the ΓXY spiral, not shown in Fig. 5) is different from the Z_2 spin liquid discovered in the Kitaev-Heisenberg model on the same lattice. The former has gapped bosonic spinon excitations and the latter supports gapless Majorana fermion excitations^{2,3}. In order

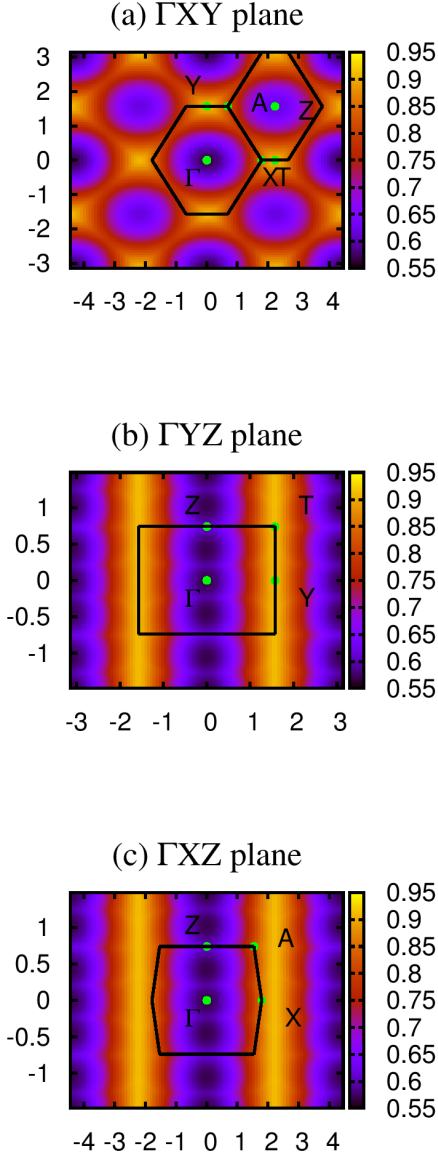


FIG. 7. (Color online) Lower edge of the two-spinon spectrum in the Z_2 spin liquid. The spectrum is calculated at $J_2/J_1 = 0.84$ and $1/\kappa = 7$ in the phase diagram of Fig. 5. Three plots show the spectra in three different planes in the first Brillouin zone: the ΓXY , ΓYZ , and ΓXZ planes.

to further characterize this Z_2 spin liquid, we show the dispersion of the lower edge of the (gapped) spinon-antispinon continuum in different planes of the Brillouin zone in Fig. 7, which can be obtained from $E_2(\mathbf{Q}) = \min_{\mathbf{p}} [\epsilon(\mathbf{Q} - \mathbf{p}) + \epsilon(\mathbf{p})]$, where $\epsilon(\mathbf{p})$ is the dispersion of the gapped bosonic excitations. Figure 7 corresponds to the case of $J_2/J_1 = 0.84$ and $1/\kappa = 7$, and the dispersions are shown for three different planes in the first Brillouin zone: ΓXY , ΓYZ , and ΓXZ

planes. The minimum energy of the two-spinon continuum occurs at $\mathbf{Q} = \pm q(1, 1, 0)$ along the ΓZ line, which is consistent with the fact that this Z_2 spin liquid emerges from the ΓZ spiral order. These dispersions of the lower edge of the spinon-antispinon continuum can, in principle, be measured in the spin structure factor via neutron scattering experiments.

V. DISCUSSION AND OUTLOOK

In this work, we investigated the nature of magnetic frustration and emergent quantum phases in the $SU(2)$ symmetric J_1 - J_2 Heisenberg model on the hyperhoneycomb lattice. We identified degenerate classical-ground-state manifold and studied the effects of quantum fluctuations. For $J_1 > 0$ and $J_2 > 0$, it was found that quantum order-by-disorder effects select spiral ordered phases as well as collinear stripy and Néel phases. Such collinear phases can be shown to be equivalent to zigzag and ferromagnetic phases when $J_1 < 0$ and $J_2 > 0$ via the transformation Eq.(2). Possible quantum spin liquid phases in the strong-quantum-fluctuation regime were also identified.

In real materials such as β - Li_2IrO_3 , magnetic anisotropies are likely to exist due to spin-orbit coupling. Hence, it is useful to investigate what the effects of such anisotropies are on magnetically ordered phases studied in this paper. While the full study of anisotropic spin interactions is beyond the scope of this paper, here we simply focus on coplanar spiral ordered phases and study how magnetic anisotropies would affect such phases. In coplanar spiral phases, the plane where the spins are lying would rotate with a pitch consistent with the ordering wavevector. Such a spiral plane is not fixed in $SU(2)$ -invariant systems and can be chosen freely. In the presence of magnetic anisotropies, however, the spiral plane may be locked to particular directions.

We now consider the spiral phases discussed in previous sections: ΓX , ΓY , and ΓZ spirals with ordering wavevectors lying along the corresponding high symmetry directions. In order to understand how the spiral plane may be constrained, we consider the Landau free energy as a function of \mathbf{d} which is defined in Eq. (3). When the system develops a spiral state with a specific ordering wavevector \mathbf{Q} , the full lattice symmetries of the hyperhoneycomb lattice are broken and only a subset of lattice symmetries remains. We use this subset of symmetries and construct the symmetry-invariant free energy (Detailed analysis is shown in Appendix D). For the ordering wavevectors lying along Γ -Z, Γ -X and Γ -Y, we denote the corresponding free energies as $f_{\Gamma Z}$, $f_{\Gamma X}$ and $f_{\Gamma Y}$, respectively. The free energies can be easily expressed in terms of a unit-vector $\hat{\mathbf{e}}_3$ normal to the spiral plane, *i.e.* $\hat{\mathbf{e}}_3 = (e_3^x, e_3^y, e_3^z) = \hat{\mathbf{e}}_1 \times \hat{\mathbf{e}}_2$:

$$\begin{aligned} f_{\Gamma Z} &= f_{\Gamma Y} = c_1 \left((e_3^x)^2 + (e_3^y)^2 \right) + c_2 \left(e_3^x e_3^y \right) \\ f_{\Gamma X} &= c_1 \left((e_3^x)^2 + (e_3^z)^2 \right) + c_2 \left(e_3^x e_3^z \right) + c_3 \left(e_3^x e_3^z + e_3^y e_3^z \right). \end{aligned} \quad (11)$$

The magnitudes of c_i ($i = 1, 2, 3$) parameters cannot be determined on symmetry grounds, thus we investigate possible directions of $\hat{\mathbf{e}}_3$ for general cases of c_i .

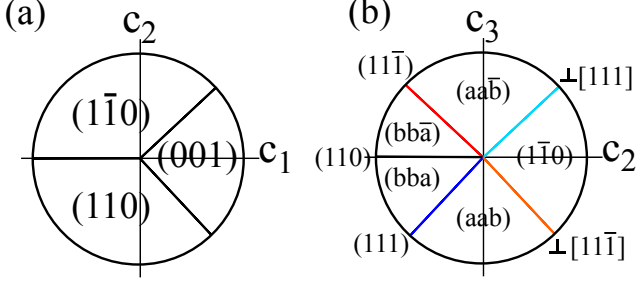


FIG. 8. Directions of \hat{e}_3 chosen by possible magnetic anisotropies, which are normal to the spiral plane. (a) and (b) show the cases of the ΓZ or ΓY spiral states and ΓX spiral state, respectively (we take the limit $c_1 = 0$ for the latter case). The symbol $\perp [111]$ indicates that any \hat{e}_3 normal to $[111]$ is possible. The parameters a and b represent continuous change of \hat{e}_3 with $b > a$. The ΓZ and ΓY spiral states select (001) , (110) and $(1\bar{1}0)$ as spiral planes, whereas, for the ΓX spiral states, the spiral plane is not completely determined and there are a number of possible choices depending on the anisotropy parameters c_i .

For the ΓZ or ΓY spiral states, there are two independent parameters c_1 and c_2 that represent possible magnetic anisotropies. Figure 8 (a) illustrates the chosen directions of \hat{e}_3 that would minimize the free energy, depending on the relative values of c_1 and c_2 . For $c_1 > 0$ and $|c_2| < c_1$, the magnetic anisotropy chooses (001) as the spiral plane, *i.e.* $\hat{e}_3 = (001)$. For $c_2 > 0$ and $c_2 > c_1$, the spiral plane is $(1\bar{1}0)$, whereas, for $c_2 < 0$ and $-c_2 > c_1$, it is (110) . Hence, one could expect that the magnetic anisotropy would make the spins to lie on any of (001) , (110) , $(1\bar{1}0)$ planes when the ΓZ or ΓY spiral states are stabilized.

On the other hand, if the ΓX spiral state is stabilized, the spiral plane is not always completely determined and some ambiguity may remain. Here one can prefer any direction as long as the components of the unit-vector \hat{e}_3 satisfy $|e_3^x| = |e_3^y|$, depending on the values of three independent parameters c_1 , c_2 and c_3 . As an example, Fig. 8 (b) illustrates the chosen directions of \hat{e}_3 for arbitrary c_2 and c_3 with $c_1 = 0$. In this case, \hat{e}_3 is pointing along the high symmetry directions only when the parameters are fine-tuned. For $c_3 = 0$, the magnetic anisotropy selects either (110) or $(1\bar{1}0)$ plane depending on the sign of c_2 . On the other hand, $(1\bar{1}0)$ plane is chosen in an extended parameter regime of finite c_3 and $c_2 > c_3$. For $c_2 < 0$ and $c_2 = \pm c_3$, the spiral plane becomes either (111) or $(11\bar{1})$. For $c_2 > 0$ and $c_2 = \pm c_3$, any spiral planes can be chosen as far as their normal vector \hat{e}_3 satisfies either $\hat{e}_3 \cdot [111] = 0$ or $\hat{e}_3 \cdot [11\bar{1}] = 0$ (We use the symbols $\perp [111]$ and $\perp [11\bar{1}]$ to represent this case in Fig. 8). Beyond these special limits, the direction of the normal vector \hat{e}_3 deviates from the high symmetry lines and sensitively changes as a function of c_i . The symbols a and b in Fig. 8 (b) indicate that the direction of \hat{e}_3 changes with $b > a$ with a and b being able to change continuously.

Finally, we discuss possible future directions related to our

results. One interesting issue would be thermal order-by-disorder effects in the same Heisenberg model on the hyperhoneycomb lattice. Similar to the effects of quantum fluctuations, thermal fluctuations may also lift the classical ground state degeneracy and select special magnetic ordering patterns. While we show that collinear magnetic orders such as the stripy phase are promoted upon including quantum fluctuations, it is not guaranteed that the entropic effect would also favour the same collinear order. In case that thermal order-by-disorder effect chooses a different state, there might be a finite temperature transition to the entropically chosen phase at finite temperatures due to the competition between quantum and thermal order-by-disorder effects. Another issue is the investigation of magnetic phases in the presence of both anisotropic spin interactions and magnetic frustration. In our paper, we mainly focused on the magnetic frustration effect and studied the $SU(2)$ -invariant Heisenberg model albeit we briefly discussed possible effects of magnetic anisotropies in spiral ordered phases. On the other hand, the full understanding of the interplay between anisotropic spin interactions and magnetic frustration may be necessary for understanding real materials. This would be an important topic for future theoretical studies.

ACKNOWLEDGMENTS

We gratefully acknowledge useful discussions with Eric Kin-Ho Lee, Subhro Bhattacharjee, and Gang Chen. We thank KIAS center for Advanced Computation for providing computing resources. This work was supported by the NSERC, CIFAR, and the Supercomputing Center/Korea Institute of Science and Technology Information with supercomputing resources including technical support (KSC-2013-C3-035). Some of the computations were performed on the gpc supercomputer at the SciNet HPC Consortium. SciNet is funded by: the Canada Foundation for Innovation under the auspices of Compute Canada; the Government of Ontario; Ontario Research Fund - Research Excellence; and the University of Toronto.

Appendix A: Hyperhoneycomb lattice structure

In this appendix, we describe the lattice structure of the three-dimensional hyperhoneycomb lattice. As shown in Fig. 1, the hyperhoneycomb lattice can be regarded as a face-centered orthorhombic Bravais lattice with a four-site basis. The primitive lattice vectors are given by

$$\mathbf{a}_1 = (2, 4, 0), \quad \mathbf{a}_2 = (3, 3, 2), \quad \mathbf{a}_3 = (-1, 1, 2), \quad (\text{A1})$$

and the coordinates of four basis vectors \mathbf{d}_α with four sublattice indices α ($\alpha = 0, 1, 2, 3$) are given by

$$\mathbf{d}_0 = (0, 0, 0), \quad \mathbf{d}_1 = (1, 1, 0), \quad \mathbf{d}_2 = (1, 2, 1), \quad \mathbf{d}_3 = (2, 3, 1). \quad (\text{A2})$$

The sites of four different sublattices are shown as distinct colored-spheres in Fig. 1. The lengths of the nearest-neighbor

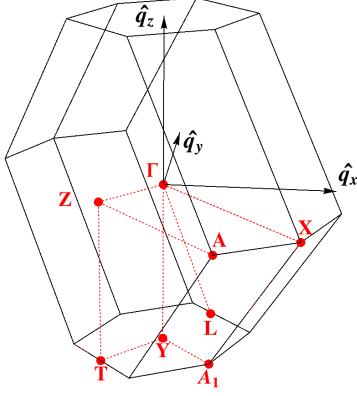


FIG. 9. (Color online) Red dots indicate high symmetric points in the Brillouin zone, and their coordinates are given by $\Gamma = (0, 0, 0)$, $Z = (-\frac{\pi}{6}, -\frac{\pi}{6}, 0)$, $T = (-\frac{\pi}{6}, -\frac{\pi}{6}, -\frac{\pi}{2})$, $X_1 = (-\frac{19\pi}{72}, -\frac{5\pi}{72}, -\frac{\pi}{2})$, $Y = (0, 0, -\frac{\pi}{2})$, $A_1 = (\frac{11\pi}{72}, -\frac{11\pi}{72}, -\frac{\pi}{2})$, $X = (\frac{29\pi}{72}, -\frac{29\pi}{72}, 0)$, $L = (\frac{\pi}{6}, -\frac{\pi}{3}, -\frac{\pi}{4})$, and $A = (\frac{13\pi}{72}, -\frac{37\pi}{72}, 0)$. Three primitive vectors of the reciprocal lattice are given by $\mathbf{b}_1 = (\frac{\pi}{3}, -\frac{2\pi}{3}, \frac{\pi}{2})$, $\mathbf{b}_2 = (-\frac{2\pi}{3}, \frac{\pi}{3}, -\frac{\pi}{2})$, and $\mathbf{b}_3 = (\frac{2\pi}{3}, -\frac{\pi}{3}, -\frac{\pi}{2})$, respectively.

and next-nearest-neighbor bonds are $\sqrt{2}$ and $\sqrt{6}$, respectively. Each sublattice site has three nearest-neighbor bonds that reside on a two-dimensional plane, forming 120° angle to each other as the case in the two-dimensional honeycomb lattice. However, unlike the honeycomb lattice, three nearest-neighbor bonds in the hyperhoneycomb lattice are not equivalent as only two of the nearest-neighbor sites belong to the same sublattice and the remaining one does not. One can also describe the lattice structure with the orthorhombic conventional unit-cell (a box in grey lines) shown in Fig. 1. Here the lattice vectors are given by $\mathbf{a} = (6, 6, 0)$, $\mathbf{b} = (-2, 2, 0)$, and $\mathbf{c} = (0, 0, 4)$ (in the same unit as used above). The reciprocal lattice vectors are given by,

$$\begin{aligned} \mathbf{b}_1 &= \left(\frac{\pi}{3}, -\frac{2\pi}{3}, \frac{\pi}{2}\right) \\ \mathbf{b}_2 &= \left(-\frac{2\pi}{3}, \frac{\pi}{3}, -\frac{\pi}{2}\right) \\ \mathbf{b}_3 &= \left(\frac{2\pi}{3}, -\frac{\pi}{3}, -\frac{\pi}{2}\right). \end{aligned} \quad (\text{A3})$$

The first Brillouin zone as well as the high symmetry directions and points are shown in Fig. 9.

Appendix B: Holstein-Primakoff linear spin-wave theory

We discuss the computation of zero-point quantum-fluctuation energy within the large- S semi-classical linear spin-wave theory. As introduced in Sec. IV A, the Holstein-Primakoff transformation in Eq. (5) leads to the spin wave Hamiltonian of the order $\mathcal{O}(S)$:

$$\begin{aligned} H_{\mathcal{O}(S)}/S &= \frac{1}{2} \sum_{ij} J_{ij} \left[a_i^\dagger a_j (\hat{\mathbf{x}}_i \cdot \hat{\mathbf{x}}_j + 1 - 2\delta_{ij} \hat{\mathbf{z}}_i \cdot \hat{\mathbf{z}}_j) \right. \\ &\quad \left. + \frac{1}{2} (a_i^\dagger a_j^\dagger + a_i a_j) (\hat{\mathbf{x}}_i \cdot \hat{\mathbf{x}}_j - 1) \right] \\ &= \sum_{\mathbf{k}, s} \left(A_{\mathbf{k}}^\dagger \ A_{-\mathbf{k}} \right) \begin{pmatrix} W_{\mathbf{k}} & T_{\mathbf{k}} \\ T_{\mathbf{k}}^{*t} & W_{-\mathbf{k}}^t \end{pmatrix} \begin{pmatrix} A_{\mathbf{k}} \\ A_{-\mathbf{k}}^\dagger \end{pmatrix} + J_m. \end{aligned} \quad (\text{B1})$$

Here, the second line denotes the Fourier-transformed Hamiltonian. $A_{\mathbf{k}}^\dagger = (a_{\mathbf{k},0}^\dagger, a_{\mathbf{k},1}^\dagger, a_{\mathbf{k},2}^\dagger, a_{\mathbf{k},3}^\dagger)$, $A_{\mathbf{k}} = (a_{\mathbf{k},0}, a_{\mathbf{k},1}, a_{\mathbf{k},2}, a_{\mathbf{k},3})$ represent boson creation, annihilation operators for sublattices 0, 1, 2 and 3 at wavevector \mathbf{k} , and $J_m = \sum_{ij} \frac{J_{ij}}{2} \hat{\mathbf{z}}_i \cdot \hat{\mathbf{z}}_j$ is the classical energy. $W_{\mathbf{k}}$ and $T_{\mathbf{k}}$ are 4×4 matrices defined as

$$\begin{aligned} (W_{\mathbf{k}})^{ss'} &= \frac{1}{16} \sum_{i \in s, j \in s'} \left(J_{ij} e^{-i\mathbf{k} \cdot (\mathbf{r}_i - \mathbf{r}_j)} [\hat{\mathbf{x}}_i \cdot \hat{\mathbf{x}}_j + 1] - 4 \delta_{s,s'} J_m \right), \\ (T_{\mathbf{k}})^{ss'} &= \frac{1}{16} \sum_{i \in s, j \in s'} \left(J_{ij} e^{-i\mathbf{k} \cdot (\mathbf{r}_i - \mathbf{r}_j)} [\hat{\mathbf{x}}_i \cdot \hat{\mathbf{x}}_j - 1] \right). \end{aligned} \quad (\text{B2})$$

Using the Bogoliubov transformation, Eq. (B1) can be rewritten in the diagonalized basis:

$$\begin{aligned} H_{\mathcal{O}(S)}/S &= \sum_{\mathbf{k}, s} \left(d_{\mathbf{k},s}^\dagger \ d_{-\mathbf{k},s} \right) \begin{pmatrix} \omega_{\mathbf{k},s} & 0 \\ 0 & \omega_{-\mathbf{k},s} \end{pmatrix} \begin{pmatrix} d_{\mathbf{k},s} \\ d_{-\mathbf{k},s}^\dagger \end{pmatrix} \\ &= \sum_{\mathbf{k}, s} 2\omega_{\mathbf{k},s} \left(d_{\mathbf{k},s}^\dagger d_{\mathbf{k},s} + \frac{1}{2} \right), \end{aligned} \quad (\text{B3})$$

where $\omega_{\mathbf{k},s}$ are the eigenvalues of $\begin{pmatrix} W_{\mathbf{k}} & T_{\mathbf{k}} \\ T_{\mathbf{k}}^{*t} & W_{-\mathbf{k}}^t \end{pmatrix} \cdot \begin{pmatrix} \mathbb{I}_4 & 0 \\ 0 & -\mathbb{I}_4 \end{pmatrix}$.

Appendix C: Mean-field ansätze for the Schwinger boson theory

Here, we describe the mean-field ansätze used in the Schwinger boson theory. As mentioned in Sec. IV B, the ansätze are translationally invariant and represented by four independent parameters η_n ($n = 1, \dots, 4$) in a unit cell. The mean-field parameters are listed in Table I for six J_1 bonds and twelve J_2 bonds in a unit cell. The four parameters are defined at four different types of bonds. The parameter η_1 (η_2) is defined for the $J_1(z)$ ($J_1(xy)$) bonds, where $J_1(z)$ connects the sublattices 0 & 1 or 2 & 3, and $J_1(xy)$ represents the rest of the J_1 -type bonds. The parameter η_3 is defined for the $J_2(xy - xy)$ bonds, where two sites in the bond are connected to two $J_1(xy)$ bonds. η_4 is defined for the $J_2(xy - z)$ bonds, where two sites in the bond are connected to $J_1(xy)$ and $J_1(z)$ bonds. The above classification of the bonds is based on lattice symmetries of the hyperhoneycomb lattice. Under lattice symmetry operations, each type of bonds are transformed into the same type of bonds, for instance a $J_1(z)$ bond is transformed to another $J_1(z)$ bond. These mean-field parameters are assumed to be real numbers.

bond	m	n	\mathbf{R}	η_{ij}
$J_1(z)$	0	1	$\mathbf{0}$	η_1
	2	3	$\mathbf{0}$	η_1
$J_1(xy)$	1	2	$\mathbf{0}$	$-\eta_2$
	3	0	\mathbf{a}_1	η_2
	3	0	\mathbf{a}_2	η_2
	2	1	\mathbf{a}_3	η_2
$J_2(xy - xy)$	0	0	$\mathbf{a}_1 - \mathbf{a}_2$	$\pm\eta_3$
	3	3	$\mathbf{a}_1 - \mathbf{a}_2$	$\pm\eta_3$
	1	1	\mathbf{a}_3	η_3
	2	2	\mathbf{a}_3	η_3
$J_2(xy - z)$	2	0	$\mathbf{0}$	η_4
	2	0	\mathbf{a}_1	η_4
	2	0	\mathbf{a}_2	η_4
	2	0	\mathbf{a}_3	η_4
	3	1	$\mathbf{0}$	η_4
	3	1	\mathbf{a}_1	η_4
	3	1	\mathbf{a}_2	η_4
	3	1	\mathbf{a}_3	η_4

TABLE I. Different types of bonds in a unit cell and mean-field ansätze $\{\eta_{ij}\}$ for the Schwinger boson mean-field theory. In the table, $i = (\mathbf{0}; m)$ and $j = (\mathbf{R}; n)$, where the first component means the lattice vector and the second the sublattice. The ansatz with the positive (negative) sign for the first half of η_3 bonds describes the ΓX (ΓY) spiral phase.

Table I describes two mean-field ansätze. Notice that the first half of η_3 bonds can have two possible signs, \pm . The ansatz with the positive (negative) sign describes the ΓX (ΓY) spiral phase.

Appendix D: Symmetry analysis of magnetic anisotropy

Here, we briefly discuss the symmetries of the hyperhoneycomb lattice following Ref. 2, and derive the symmetry transformation properties of the order parameter \mathbf{d} , defined in Eq. (3). The ideal hyperhoneycomb lattice is described by the space group $Fddd$ and the point group D_{2h} . There are three types of symmetry operations in the hyperhoneycomb lattice

(See Fig. 1):

1. Inversion at the bond center of sublattices 1 and 2, or sublattices 0 and 3.
2. Three orthogonal C_2 axes at the bond center of sublattices 0 and 1, or sublattices 2 and 3. These axes are parallel to the lattice vectors \mathbf{a} , \mathbf{b} and \mathbf{c} of the underlying face-centered orthorhombic Bravais lattice (defined in Appendix A).
3. Glide planes parallel to each face of the orthorhombic unit-cell followed by translation $\mathbf{a}_i/2$ (defined in Appendix A).

There are four generators for D_{2h} point group: inversion \mathcal{I} and three C_2 rotations, C_{2a} , C_{2b} , C_{2c} . Using these four generators, one can examine how the spin \mathbf{S}_i [Eq. (3)], that is a pseudo-vector, transforms under each symmetry operation.

We consider two different types of spiral states: ΓZ spiral state with the ordering wavevector $\mathbf{Q} = q(1, 1, 0)$ and ΓXY spiral state with the ordering wavevector, either $\mathbf{Q} = q(1, \bar{1}, 0)$ or $\mathbf{Q} = q(0, 0, 1)$. For $0.17 < J_2/J_1 < 0.5$, the ground state is the ΓZ spiral state with the ordering wavevector $\mathbf{Q} = q(1, 1, 0)$ and the corresponding little group (for the remaining lattice symmetries) is generated by \mathcal{I} , C_{2a} . Under the symmetry operations, the order parameter \mathbf{d} transforms as

$$\begin{aligned} \mathcal{I} : \mathbf{d} &\rightarrow \mathbf{d}^* \\ C_{2a} : d_x &\rightarrow d_y, d_y \rightarrow d_x, d_z \rightarrow -d_z. \end{aligned} \quad (\text{D1})$$

Similarly, for $J_2/J_1 > 0.5$, the ground state is the ΓXY spiral state with the ordering wavevector, either $\mathbf{Q} = q(1, \bar{1}, 0)$ or $\mathbf{Q} = q(0, 0, 1)$. For the case of the ordering wave vector $\mathbf{Q} = q(1, \bar{1}, 0)$, the little group is generated by \mathcal{I} , C_{2b} and the order parameter \mathbf{d} transforms as

$$\begin{aligned} \mathcal{I} : \mathbf{d} &\rightarrow \mathbf{d}^* \\ C_{2a} : d_x &\rightarrow -d_y, d_y \rightarrow -d_x, d_z \rightarrow -d_z. \end{aligned} \quad (\text{D2})$$

In the case of the ordering wavevector $\mathbf{Q} = q(0, 0, 1)$, the little group is generated by \mathcal{I} , C_{2c} . The order parameter \mathbf{d} transforms under these symmetries as follows.

$$\begin{aligned} \mathcal{I} : \mathbf{d} &\rightarrow \mathbf{d}^* \\ C_{2c} : d_x &\rightarrow -d_y, d_y \rightarrow -d_x, d_z \rightarrow d_z. \end{aligned} \quad (\text{D3})$$

Based on these symmetry-transformation properties of the order parameter \mathbf{d} , one can figure out the symmetry-allowed Landau free energy in terms of \mathbf{d} as shown in Eq. (12).

¹ H. Takagi, Talk at the Conference on *Spin Orbit Entanglement: Exotic States of Quantum Matter in Electronic Systems*, MPIPES, Dresden (July 22-July 26, 2013).

² E. K.-H. Lee, R. Schaffer, S. Bhattacharjee, and Y. B. Kim, *Phys. Rev. B* **89**, 045117 (2014).

³ I. Kimchi, J. G. Analytis, and A. Vishwanath, ArXiv e-prints (2013), [arXiv:1309.1171 \[cond-mat.str-el\]](https://arxiv.org/abs/1309.1171).

⁴ S. Lee, E. K.-H. Lee, A. Paramakanti, and Y. B. Kim, *Phys. Rev. B* **89**, 014424 (2014).

⁵ G. Jackeli and G. Khaliullin, *Phys. Rev. Lett.* **102**, 017205 (2009).

⁶ Y. Singh and P. Gegenwart, *Phys. Rev. B* **82**, 064412 (2010).

⁷ D. Pesin and L. Balents, *Nature Physics* **6**, 376 (2010).

⁸ B.-J. Yang and Y. B. Kim, *Phys. Rev. B* **82**, 085111 (2010).

⁹ W. Witczak-Krempa and Y. B. Kim, *Phys. Rev. B* **85**, 045124 (2012).

- ¹⁰ J. Chaloupka, G. Jackeli, and G. Khaliullin, *Phys. Rev. Lett.* **105**, 027204 (2010).
- ¹¹ X. Liu, T. Berlijn, W.-G. Yin, W. Ku, A. Tsvelik, Y.-J. Kim, H. Gretarsson, Y. Singh, P. Gegenwart, and J. P. Hill, *Phys. Rev. B* **83**, 220403 (2011).
- ¹² Y. Singh, S. Manni, J. Reuther, T. Berlijn, R. Thomale, W. Ku, S. Trebst, and P. Gegenwart, *Phys. Rev. Lett.* **108**, 127203 (2012).
- ¹³ W. Witczak-Krempa, G. Chen, Y. B. Kim, and L. Balents, *Condensed Matter Physics* **5** (2013).
- ¹⁴ H. Gretarsson, J. P. Clancy, X. Liu, J. P. Hill, E. Bozin, Y. Singh, S. Manni, P. Gegenwart, J. Kim, A. H. Said, D. Casa, T. Gog, M. H. Upton, H.-S. Kim, J. Yu, V. M. Katukuri, L. Hozoi, J. van den Brink, and Y.-J. Kim, *Phys. Rev. Lett.* **110**, 076402 (2013).
- ¹⁵ R. Comin, G. Levy, B. Ludbrook, Z.-H. Zhu, C. N. Veenstra, J. A. Rosen, Y. Singh, P. Gegenwart, D. Stricker, J. N. Hancock, D. van der Marel, I. S. Elfimov, and A. Damascelli, *Phys. Rev. Lett.* **109**, 266406 (2012).
- ¹⁶ J. Dai, E. Calleja, G. Cao, and K. McElroy, *arXiv preprint arXiv:1303.3688* (2013).
- ¹⁷ H. Kuriyama, J. Matsuno, S. Niitaka, M. Uchida, D. Hashizume, A. Nakao, K. Sugimoto, H. Ohsumi, M. Takata, and H. Takagi, *Applied Physics Letters* **96**, 182103 (2010).
- ¹⁸ S. K. Choi, R. Coldea, A. N. Kolmogorov, T. Lancaster, I. I. Mazin, S. J. Blundell, P. G. Radaelli, Y. Singh, P. Gegenwart, K. R. Choi, S.-W. Cheong, P. J. Baker, C. Stock, and J. Taylor, *Phys. Rev. Lett.* **108**, 127204 (2012).
- ¹⁹ J. Chaloupka, G. Jackeli, and G. Khaliullin, *Phys. Rev. Lett.* **110**, 097204 (2013).
- ²⁰ A. Kitaev, *Annals of Physics* **321**, 2 (2006).
- ²¹ Z. Nussinov and J. van den Brink, *ArXiv e-prints* (2013), [arXiv:1303.5922 \[cond-mat.str-el\]](https://arxiv.org/abs/1303.5922).
- ²² I. Kimchi and Y.-Z. You, *Phys. Rev. B* **84**, 180407 (2011).
- ²³ K. Foyevtsova, H. O. Jeschke, I. I. Mazin, D. I. Khomskii, and R. Valentí, *Phys. Rev. B* **88**, 035107 (2013).
- ²⁴ S. Mandal and N. Surendran, *Phys. Rev. B* **79**, 024426 (2009).
- ²⁵ J. Nasu, T. Kaji, K. Matsuura, M. Udagawa, and Y. Motome, *ArXiv e-prints* (2013), [arXiv:1309.3068 \[cond-mat.str-el\]](https://arxiv.org/abs/1309.3068).
- ²⁶ M. Hermanns and S. Trebst, *ArXiv e-prints* (2014), [arXiv:1401.7678 \[cond-mat.str-el\]](https://arxiv.org/abs/1401.7678).
- ²⁷ E. K.-H. Lee, S. Bhattacharjee, K. Hwang, H.-S. Kim, H. Jin, and Y. B. Kim, *arXiv preprint arXiv:1402.2654* (2014).
- ²⁸ D. H. Lyons, T. A. Kaplan, K. Dwight, and N. Menyuk, *Phys. Rev.* **126**, 540 (1962).
- ²⁹ J. M. Luttinger and L. Tisza, *Phys. Rev.* **70**, 954 (1946).
- ³⁰ J. M. Luttinger, *Phys. Rev.* **81**, 1015 (1951).
- ³¹ D. Bergman, J. Alicea, E. Gull, S. Trebst, and L. Balents, *Nature Physics* **3**, 487 (2007).
- ³² S. Lee and L. Balents, *Phys. Rev. B* **78**, 144417 (2008).
- ³³ E. F. Shender, *Sov. Phys JETP* **56**, 178 (1982).
- ³⁴ C. L. Henley, *Phys. Rev. Lett.* **62**, 2056 (1989).
- ³⁵ J. Alicea, A. V. Chubukov, and O. A. Starykh, *Phys. Rev. Lett.* **102**, 137201 (2009).
- ³⁶ D. P. Arovas and A. Auerbach, *Phys. Rev. B* **38**, 316 (1988).
- ³⁷ N. Read and S. Sachdev, *Phys. Rev. Lett.* **66**, 1773 (1991).
- ³⁸ S. Sachdev, *Phys. Rev. B* **45**, 12377 (1992).
- ³⁹ O. Tchernyshyov, R. Moessner, and S. Sondhi, *EPL* **73**, 278 (2006).